ACCSCIENCE PUBLISHING

Materials Science in Additive Manufacturing

ORIGINAL RESEARCH ARTICLE

Gaussian process-based interpretable prediction of melt track morphology through melt pool in additive manufacturing

Xin Lin[1], Shilin Liu[1], Haodong Chen[1], Jinrong Mao[1], and Kunpeng Zhu[1,2]*

[1]Precision Manufacturing Institute, Wuhan University of Science and Technology, Wuhan, Hubei, China

[2]Institute of Intelligent Machines, Hefei Institutes of Physical Science, Chinese Academy of Sciences, Hefei, Anhui, China

(This article belongs to the *Special Issue: Smart Additive Manufacturing: Product and Process Qualification through Innovation in Design, Modeling, Monitoring, Machine Learning, Metrology, and Materials Science*)

Abstract

Melt track monitoring in the laser powder bed fusion (LPBF) process is crucial for preventing internal defects in as-printed parts. Uncontrollable melt pool dynamic behavior easily leads to melt track morphology defects. Existing monitoring methods face challenges in balancing modeling accuracy and physical interpretability. Specifically, traditional physics-based models typically require complex monitoring equipment, extensive simulation data, and empirical formulas, resulting in high costs and limited applicability. Meanwhile, conventional data-driven models lack physical constraints, leading to insufficient interpretability, process parameter sensitivity, and poor generalization. To address these challenges, this article proposes a deep Gaussian process-based method for LPBF melt track morphology prediction. The proposed model employs kernel functions in the first layer to learn melt pool evolution patterns and embeds the Rosenthal equation into the second-layer kernel function as a physical constraint, constructing a physically interpretable multilayer Gaussian process framework. Finally, a softmax classifier based on melt track geometric deviation achieves five-category melt track morphology recognition. Multi-condition experimental results demonstrated that the proposed method achieved root mean square errors of 0.069, 0.020, and 0.039 for melt track geometry, outperforming traditional data-driven models in prediction accuracy. The classification accuracy reached 90.76%. Furthermore, the influence of different features on melt track morphology is quantified through time-lagged mutual information analysis and other visualization methods. This study provides an effective solution for achieving quality monitoring and defect prediction in the LPBF process.

Keywords: Laser powder bed fusion; Deep Gaussian process; Morphology prediction; Physical constraint; Melt pool monitoring

***Corresponding author:**
Kunpeng Zhu
(zhukp@iamt.ac.cn)

Citation: Lin X, Liu S, Chen H, Mao J, Zhu K. Gaussian process-based interpretable prediction of melt track morphology through melt pool in additive manufacturing. *Mater Sci Add Manuf.* 2025;4(3):025200030. doi: 10.36922/MSAM025200030

Received: May 12, 2025

Revised: June 5, 2025

Accepted: June 8, 2025

Published online: July 17, 2025

1. Introduction

Additive manufacturing (AM) technology has made remarkable developments in the manufacturing field in recent years and is an innovative approach that surpassed

traditional manufacturing methods. However, the complex changes in the AM process, such as heat transfer, melting, and solidification processes,[1] are prone to cause defects, such as holes, cracks, and unfused parts, limiting the reliability of AM technology in production applications. To address this issue, the introduction of remote and *in situ* monitoring techniques is critical. By continuously monitoring the manufacturing process, tracking key physical phenomena during fusion, and analyzing real-time data from various sensors, this approach enabled the detection of defects before they become hidden beneath subsequent layers.[2-5]

At present, AM process monitoring primarily relies on analyzing in-process sensor data through data modeling, using machine learning and deep learning to detect specific defect occurrences. For example, Khanzadeh *et al.*[6,7] analyzed the thermal distribution characteristics of the melt pool and successfully predicted both pore locations in Ti-6Al-4V alloy parts and geometric deviations in the Fast Fourier Transform process using self-organizing mapping (an unsupervised learning algorithm); they also investigated the influence of process parameters on geometric accuracy. Scime *et al.*[8] classified the types of anomalies in the melt track into six categories and proposed a monitoring algorithm based on machine learning and computer vision, which was successfully used for *post hoc* quality analysis of components. Okaro *et al.*[9] applied binary labels to a small data subset based on defect severity and developed a semi-supervised model using process data with singular value decomposition and Gaussian mixture models. This approach achieved classification performance comparable to fully supervised methods. Yuan *et al.*[10,11] proposed a two-round image processing and height map analysis algorithm to predict and identify laser printing track width and continuity in video datasets. Their approach considered the characteristics of diverse data and addressed labeling difficulties using semi-supervised learning. Mojahed Yazdi *et al.*[12] designed a deep neural network model that utilizes the spatial feature image of regions of interest (ROI) to detect and locate defects. This method achieved significantly higher defect detection rates than traditional machine learning approaches. Lopez *et al.*[13] focused more on quantifying model uncertainty. They explored melt pool width prediction by considering uncertainties arising from thermal modeling assumptions, unknown simulation data, numerical approximations, and calibration data. While these studies leverage the power of machine learning and deep learning to establish complex mapping relationships between monitoring data and melt track geometry, such prediction methods often lack physical interpretability. In addition, they can be highly sensitive to experimental parameters and exhibit limited generalization ability.

In recent years, more researchers explored combining physical models with data models to improve the performance and generalization ability of the models by adding physical constraints. For example, Mahmoudi *et al.*[14] proposed an anomaly detection system that integrated melt pool and phase field models. Utilizing high-speed thermal imaging, spatial statistics, and machine learning, their approach achieved only a 5% average error in melt track width prediction. Gaikwad *et al.*[15] obtained the physical characteristics of the melt pool by utilizing different sensors, such as high-speed cameras and thermocouples, and employed neural networks to predict melt pool patterns, process parameters, melt track width, and melt track continuity. Guo *et al.*[16] established a mathematical melt pool morphology model by fitting key coefficients through extensive experiments. Their model accounts for physical mechanisms, including mass conversion, heat exchange, and temperature fields, thereby controlling average prediction errors for melt pool dimensions (length/width/depth) to 12%. Zhang *et al.*[17] fused melt pool spatial-physical information through coaxial/off-axis dual detection systems. Using long short-term memory networks, they correlated the melt pool temperature with melt track surface morphology, achieving up to 92.87% accuracy. These researchers obtained multimodal data through a large number of experiments and a variety of high-precision sensors and realized the identification of melt pool geometry and anomalous states by combining physical processes.

Based on these findings, traditional physical models incur high experimental costs due to complex monitoring equipment, extensive simulation data, and empirical formulas. Conversely, traditional data-driven models lack physical constraints, exhibit high sensitivity to process parameters, and are susceptible to noise interference. To address these limitations, we propose a melt track morphology prediction model based on deep Gaussian processes (DGPs) with embedded physical constraints. DGPs are a multilayer generalization of Gaussian processes (GPs),[18] where each layer is an independent GP. Compared to single-layer GPs, DGPs overcome the limited expressiveness of the kernel function and also maintain the flexibility, overfitting resistance, and good prediction uncertainty of the GP model. In this study, the experimentally observed melt pool geometric feature data were used as model inputs, with physical model constraints added to the data-driven DGP model to guide physical information to the data model. This approach enables the prediction of geometric features of the melt track and the classification of the morphology of the melt track under different processing conditions using a softmax classification model. The structure of the proposed model is displayed in Figure 1.

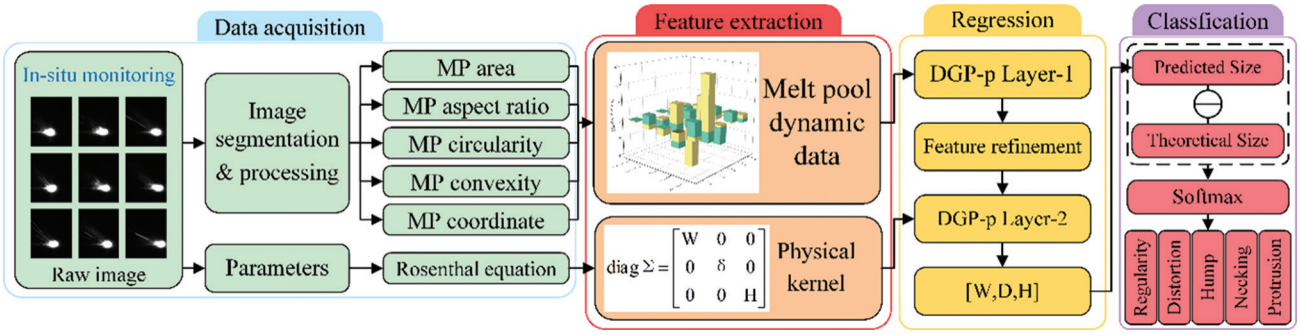

Figure 1. Geometric prediction and morphology classification model of the melt track based on DGP and softmax
Abbreviations: MP: Melt pool; DGP-p: DGP model using physical kernel; W: Melt track width; δ: Small perturbation; H: Melt track height

2. Experiment and methods

2.1. Experimental setup

In this study, the laser powder bed fusion (LPBF) system was set up based on existing LPBF equipment for modification, incorporating high-speed cameras, zoom lenses, and other auxiliary monitoring equipment. The high-speed monitoring system was mounted on the side axis to avoid interference from the laser shielding glass on the molding chamber door, which could affect the imaging results (Figure 2). The laser spot radius of the LPBF equipment was 0.05 mm. The sampling frame rate (FR) of the high-speed camera was calculated to be 10,600 fps using Equation I based on a maximum scanning speed of 1,060 mm/s. The sampling FR was set to 10,000 fps instead of the calculated 10,600 fps for the convenience of calculation.

$$FR = \frac{V}{2r} \quad \text{(I)}$$

Where V denotes the laser scanning speed (mm/s) and r denotes the laser spot radius (mm).

In this experiment, 316L stainless steel powder (particle size: 15 – 45 μm) was uniformly coated on a substrate, whose base material was also 316L stainless steel, using a squeegee, with the layer thickness set to 0.04 mm and the scanning length set to 3 mm. The experimental protocol included five types of laser power (140, 190, 240, 290, and 340 W) and five types of scanning speeds (0.66, 0.76, 0.86, 0.96, and 1.06 m/s), totaling 25 combinations.[19,20] We collected a total of 932 samples.

Figure 3 illustrates the specific distribution of melt track morphology, which was then oversampled by a factor of 2 using the Synthetic Minority Oversampling Technique (SMOTE) during classification prediction due to the significant imbalance in the defect categories.

According to the high-speed camera FR f = 10000 fps and the melt track length L_{total} = 3 mm, for different

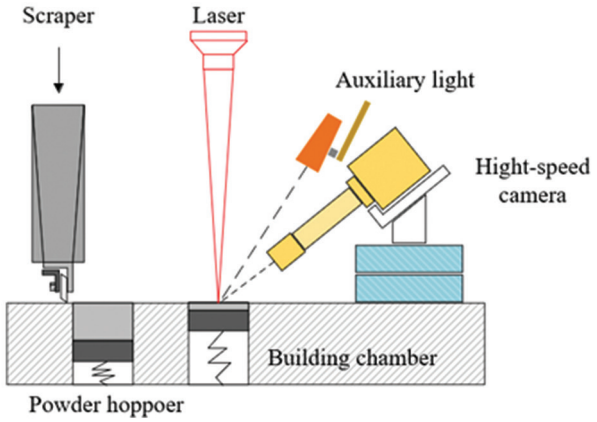

Figure 2. Schematic diagram of the axis monitoring system next to the melt pool

laser scanning speeds v (m/s), the number of melt pool pictures $n = f. L_{total}/v$ was generated, and the corresponding melt track would be sliced in equal portions according to n. The average width of the segment, W_{mean}, average deviation D_{mean}, and average height H_{mean} were obtained by sampling each slice using 7/10n (rounded) points. The schematic diagram for extracting the respective melt track characteristics is presented in Figure 4. The data were retained to two decimal places.

The DGP regression model and softmax classifier were applied to 25 datasets – 3 datasets served as the test set and 22 datasets served as the training set – to establish the relationship between the melt pool geometric features, process parameters, and melt track features, as well as to predict the melt track geometric features and the morphology category. Since a small sample dataset was used, the results of dataset division accounted for a large influence on the model performance. Finally, the dataset was split into an 18:4:3 ratio – 18 datasets were used for model training, 4 datasets served as the validation set, and 3 datasets (240 W-660 mm/s, 290 W-760 mm/s, and 340 W-960 mm/s) were randomly selected as the test sets.

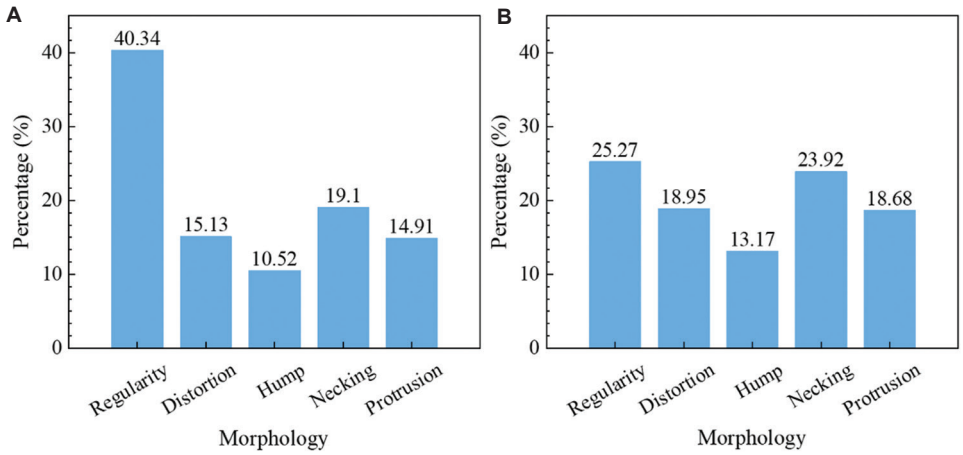

Figure 3. Category distribution: (A) without oversampling, and (B) with oversampling

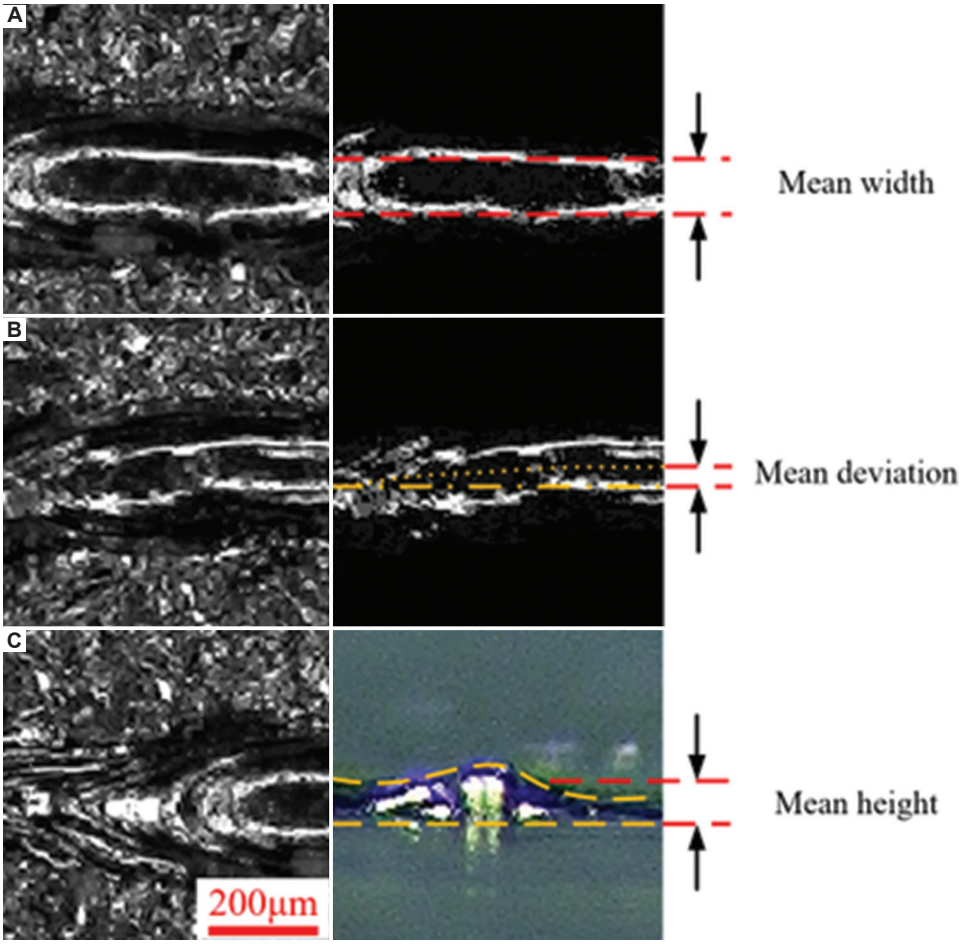

Figure 4. Extraction of melt track features: (A) mean width, (B) mean deviation, and (C) mean height. Scale bar: 200 μm

2.2. Defects in the melt track

In the LPBF process, the flow state of the melt has a great influence on the shape of the melt pool.Numerous studies have established a clear relationship between melt pool characteristics and various types of defects.[21] Drastic changes

in the melt pool can lead to defects in the trajectories. Five types of trajectory characteristics—regularity, distortion, hump, necking, and protrusion—were identified in the experiments, and their morphologies are displayed in Figure 5.

Figure 5A displays a regularity-shaped melt track, characterized by continuous edges that do not deviate from the preset scanning path and are symmetrical along the centerline of the scanning trajectory. Figure 5B features a distortion-shaped melt track,[22] which usually has continuous edges, but the center of the melt track deviates from the pre-defined scanning path, probably due to the Marangoni effect that distorts the trajectory. Figure 5C presents a hump-shaped melt track,[23] which usually has different thicknesses due to bulging. This is associated with the Plateau-Rayleigh (P-R) instability generated by the pressure difference acting on the surface of the melt pool.[24] Figure 5D illustrates a melt track with necking-shaped morphology,[25] characterized by a contraction in width or even the appearance of breakpoints – a phenomenon that is also believed to be caused by cylindrical fluid jets. Figure 5E features a protrusion-shaped melt track,[26] often accompanied by a sudden increase in width, forming an angular lateral bulge – a phenomenon that is usually attributed to high surface tension melt pools and the Marangoni effect.[27]

2.3. Data processing

High surface tension makes the melt pool surface unstable, which can easily lead to melt rupture. The Marangoni effect induces the melt to flow from the high-temperature region to the low-temperature region, leading to metal splashing from the surface of the melt pool. When the surface of the melt pool is disturbed by the expansion, the P-R instability makes the surface of the melt pool protrude, which leads to the splitting of the melt and the splashing of the melt. The combined effect of these factors on the melt pool leads to drastic changes in the morphology of the melt pool, thus increasing the risk of defects.[28,29]

To fully characterize the melt pool geometry, quantitative analysis was performed by extracting geometrical parameters, such as aspect ratio, roundness, and convex defects of the melt pool. During the LPBF process, images captured by the high-speed camera in the side-axis monitoring system are subject to interference from intense metal powder splatter, plasma plumes, and substrate surface reflections. To address this, the ROI method was first applied to identify the maximum connected region (128 × 128 pixels) with grayscale values exceeding 200. This approach effectively eliminates most splatter interference while preserving the integrity of the melt pool morphology. Second, the k-means segmentation method (segmentation category: 7; i.e., the category with the largest sum of pixel values) was used to remove the plume, proximity powder splash, and metal material arc light, among other parameters. The large particle droplet splash and the melt pool were then separated by the kernel operation (kernel size: 5). Connectivity domain analysis was then used to select the largest area to obtain the main body of the melt pool. According to the main body, the area s_m, perimeter p_m, convexity defect t_m, length l_m, width w_m, and center of mass coordinates x,y of the melt pool were calculated, and the flow is displayed in Figure 6. The input features $x_m = [s_m, ar_m, c_m, t_m, y]$ of the melt pool were obtained based on Equations II and III.

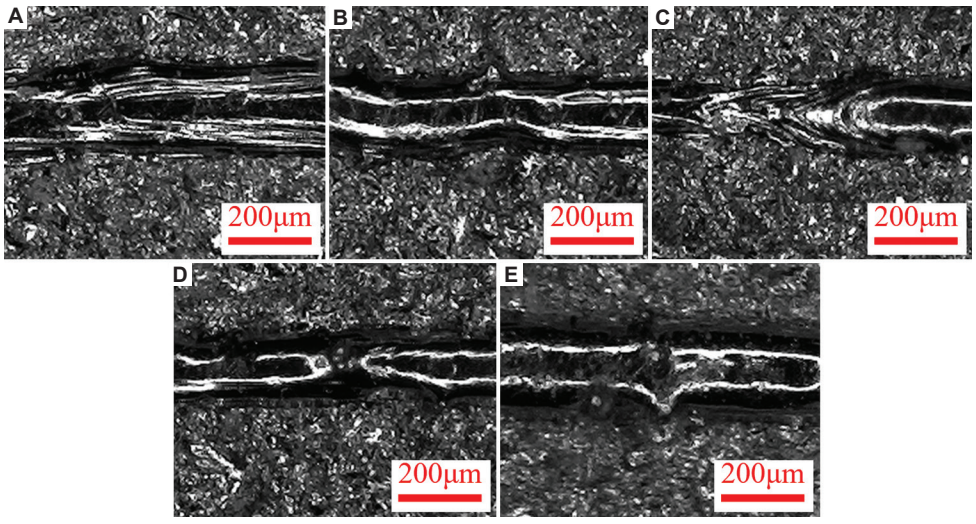

Figure 5. Five different types of melt track morphology in laser powder bed fusion: (A) regularity, (B) distortion, (C) hump, (D) necking, and (E) protrusion. Scale bar: 200 μm

$$ar_m = l_m / w_m \quad \text{(II)}$$

$$c_m = 4\pi s_m / p_m \quad \text{(III)}$$

The oscillatory motion of the melt pool is induced by the combined effects of thermocapillary force, recoil pressure, and surface tension.[30] After extracting the shape characteristics of the melt pool, the characteristic difference between the melt pool at the experimentally observed melt track defects and the neighboring time steps was calculated for the melt pool using Equation IV.

$$\begin{cases} \Delta_m^t = (x_m^t - x_m^{t-1}) / x_m^t \\ \Delta_m^{t+1} = (x_m^t - x_m^{t+1}) / x_m^t \end{cases} \quad \text{(IV)}$$

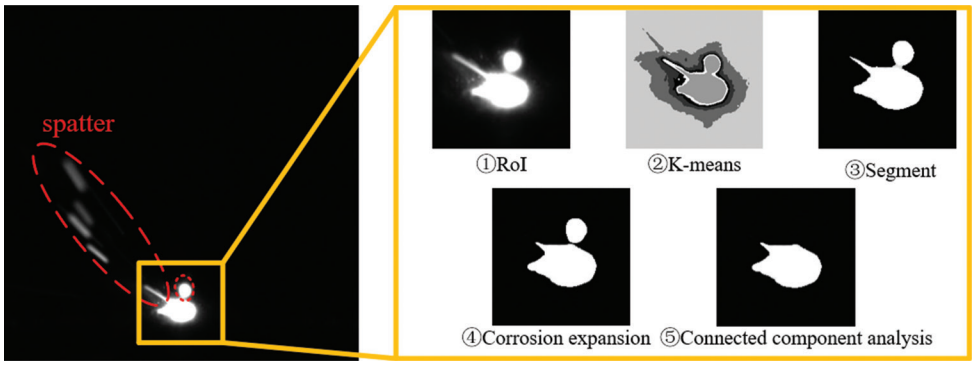

Figure 6. Extraction of melt pool features
Abbreviation: ROI: Region of interest

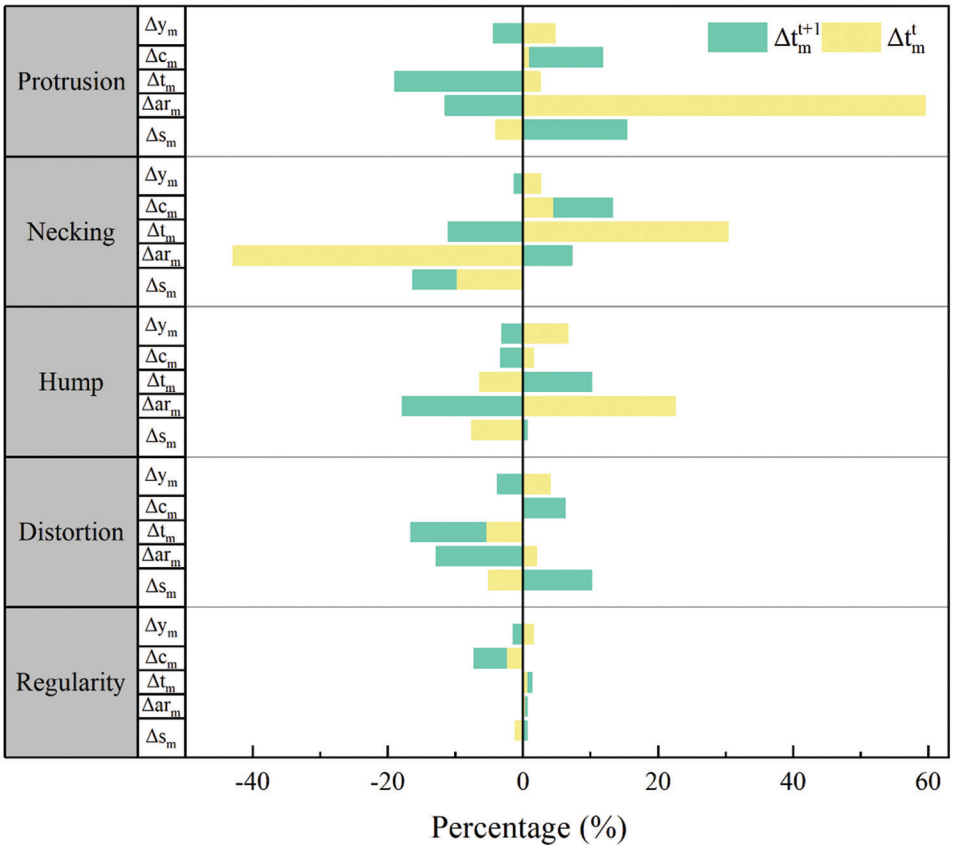

Figure 7. Changes in melt pool characteristics
Abbreviations: y_m: Y-coordinate of the melt pool centroid; c_m: Roundness of the melt pool; t_m: Convex defects in the melt pool; ar_m: The aspect ratio of the melt pool; s_m: The area of the melt pool

The statistical results are presented in Figure 7.

From Figure 8, it can be seen that the regular morphology has stable geometric features, corresponding to a small change in the geometric features of the melt pool. For melt track defects involving width distortion, such as necking and protrusion, the melt pool morphology exhibits distinct changes. During necking, the melt pool area and aspect ratio decrease significantly. Conversely, during protrusion, the melt pool area, aspect ratio, and convexity increase significantly. Therefore, the melt track width may be determined by a combination of the melt pool area, aspect ratio, and convex defects.

For defects in which the melt track deviates from the preset scanning path (i.e., distorted morphology), the area of the melt pool and the y-axis coordinates of the center of mass change significantly, and the extent of the deviation of the melt track may be jointly determined by the area of the melt pool and the y-axis coordinates of the center of mass.

For defects with distortion in the height of the melt track (i.e., hump shape), the area of the melt pool decreases and the aspect ratio increases. The upward shift of the center of mass of the melt pool indicates an increase in the height of the melt track, which may be due to the limitation of the viewing angle of the monitoring equipment. The change in the area and width of the actual melt pool needs to be further verified.

2.4. Melt track theory model

Existing studies[31-34] on 316L, Ti-6Al-4V, and Inconel718 materials have consistently demonstrated that powder bed coverage has no significant effect on melt pool width. Guo *et al.*[16] also verified that, in the case of ignoring the random spattering and flaking of powder, it can be assumed that the powder consumption width and the melt track width are approximately equal. Therefore, this study assumes that the powder consumption width is equal to the theoretical track width.

Assuming that the upper profile curve of the melt track above the substrate surface is bow-shaped (Figure 9A), for points on the curve (x_0,y_0) to meet the center of the circle $(0,y_R)$, the radius R[35,36] can be expressed as Equation V.

$$x_o^2 + (y_o - y_R)^2 = R^2 \quad \text{(V)}$$

Based on the conservation of mass, Equation VI is derived. Similarly, based on the bowing geometry, a relationship can be derived between the width W, radius R, height H, and the bowing area (Equations VII and VIII).

$$\rho_{powder}\, LWL_{track} = \rho LA_{track} \quad \text{(VI)}$$

$$W = 2\sqrt{2RH - H^2} \quad \text{(VII)}$$

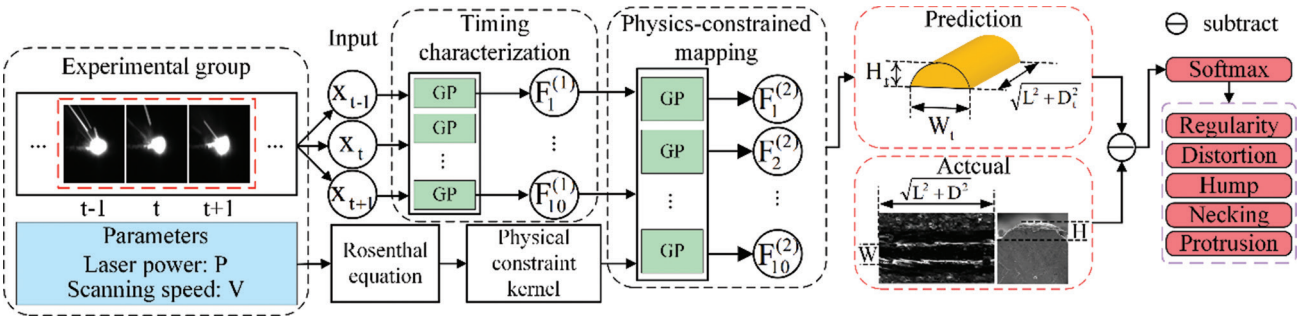

Figure 8. The deep Gaussian process DGP model using the physical kernel (DGP-p) model

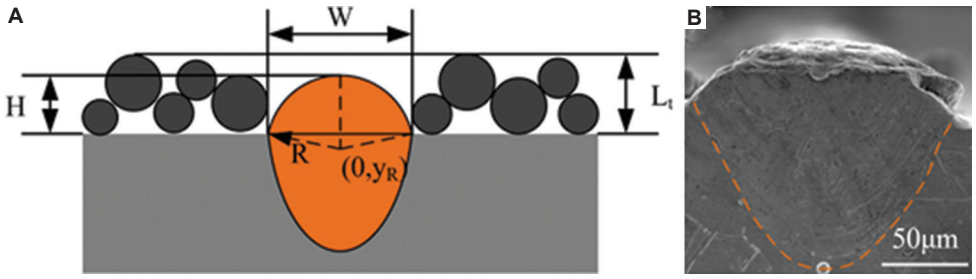

Figure 9. Shape of melt track. (A) Schematic diagram of theoretical melt track. (B) Image of actual melt track
Abbreviations: H: melt track height; W: Melt track width; L_t: Powder layer thickness; R: Radius of the circular contour on the melt track's upper surface; y_R: Y-coordinate of the center point of the melt track's upper surface contour

$$A_{track} = R^2 \arccos\left(\frac{R-H}{R}\right) - (R-H)\sqrt{2RH-H^2} \quad \text{(VIII)}$$

Where W and H denote the width and height of the melt track; R denotes the radius of the bowls; A_{track} denotes the area of the upper half of the melt track; ρ_{powder} and ρ denote the powder material density and single-pass material density, respectively; L_{track} denotes the layer thickness; and L, W, and H denote the length, width, and height of the upper partial melt track.

In this study, the powder's stacking density was assumed to be 50%; that is, ρ_{powder} = 50% ρ, where ρ is the material density, which is taken as 7,800 kg/m^3.

By substituting Equation VII into Equation VI and associating it with Equation VIII, Equation IX is obtained.

$$0.5WL_{track} = \left(\frac{W^2+4H^2}{8H}\right)^2 \arccos\left(1-\frac{8H^2}{W^2+4H^2}\right) - \left(\frac{W^2+4H^2}{8H}-H\right)\frac{W}{2} \quad \text{(IX)}$$

Using Halley's iterative method, the melt track height H can be solved. However, for the melt track width W, it has been indicated that the effect of laser radius on the melt track width is negligible.[16] The width of the melt track based on the formation of the melt track by the steady-state melt pool can be expressed as Equation X.

$$\xi P = 2\pi k(T_f - T_0)W + 0.1 \bullet e\pi\rho C\,(T_f - T_0)\,VW^2 \quad \text{(X)}$$

Where the powder absorption rate ξ is taken as 0.35; P is the laser power; π is the circumference; the thermal conductivity k is taken as 14 W/m K; the initial temperature T_0 is taken as 300 K; the melting temperature T_f of the powder is taken as 1700 K; e is a natural constant; the specific heat capacity C is taken as 683 J/kg K; and V is the laser scanning speed.

Similarly, the theoretical volume of the melt track *Vol* is expressed in Equation XI.

$$Vol = \left(\frac{\pi W^2}{4} - \frac{1}{2}WH\right)L \quad \text{(XI)}$$

2.5. DGP-p-based melt track size prediction and morphology classification

DGPs have a powerful non-linear learning capability, with a network structure that consists of an input layer, a hidden layer, and an output layer (Figure 8).

For the melt pool, the geometric feature vector $x_m = [s_m, ar_m, c_m, t_m, y]$ at time t is normalized based on the melt pool features of the neighboring moments. The feature matrix $X_t = [x_m^{t-1}, x_m^t, x_m^{t+1}]^T$ is formed as the input, while the hidden layer is defined by the melt track features $Y_t = [W_t, D_t, H_t]$. The process flow is displayed in Figure 8. Due to the general complexity of the experimental data in this study, a two-layer DGP model was used, containing the following core layers:

(i) Melt pool periodic feature extraction layer (first layer): For the melt pool data of the same test set, 10 independent GPs – each using the Gaussian cosine composite kernel function – were used two-by-two to learn the characteristic fluctuations of different frequencies. For the input of melt pool time series data X_t, the output $F_i^{(1)}(X_t)$ of the ith GP obeys the following distribution (Equation XII).

$$F_i^{(1)} \sim GP\left(\mu_i^{(1)}(X_t), K^{(1)}(X_t, X_t')\right),\ i = 1,\ldots,10 \quad \text{(XII)}$$

The work of Salimbeni *et al.*[37] also indicated that the linear mean function predicts better than the constant mean function, and the computational overhead is less than that of the non-linear mean function; hence, each GP mean function $\mu_i^{(j)}(X)$ is in linear form (Equation XIII).

$$\mu_i^{(1)}(x_m) = a_i^T x_m,\ i = 1,\ldots,10 \quad \text{(XIII)}$$

Where $K^{(1)}(X_t, X_t')$ is expressed as in Equation XIV.

$$K^{(1)}(X_t, X_t') = \sigma_i^2 exp\left(-\frac{X_t - X_t'^2}{2l_i^2}\right) \cdot cos\left(\frac{2\pi X_t - X_t'}{T_i}\right),\ i = 1,\ldots,10\# \quad \text{(XIV)}$$

Where σ_i^2 is used to control the amplitude of the output of the kernel function, l_i^2 is used to control the smoothness of the kernel, and T_i defines the periodicity of the function.

(ii) Melt track geometric feature mapping layer (second layer): This layer maps the periodic feature $F^{(1)}$ output from the first layer to the melt track geometric feature $F^{(2)}$ through six GPs. Each GP uses the Matérn kernel employing physical constraints, and for the jth GP, the output $F_j^{(2)}(x)$ obeys the following distribution (Equations XV and XVI).

$$F_j^{(2)} \sim GP\left(\mu_j^{(2)}(F^{(1)}), K^{(2)}(F^{(1)}, F^{(1)'})\right),\ j = 1,\ldots,6 \quad \text{(XV)}$$

$$K^{(2)}(F^{(1)}, F^{(1)'}) = \sigma_m^2 \exp(-\frac{1}{2}(F^{(1)} - F^{(1)'})^T £^{-1}(F^{(1)} - F^{(1)'})) \quad \text{(XVI)}$$

Where σ_m^2 is the magnitude, Σ = diag ([W^2, δ, H^2]), and δ is a small perturbation term to prevent the theory from deviating from 0 and causing numerical instability.

Finally, the geometrical parameter $Y_t = \sum_{j=1}^{6} w_j K_j^{(2)}\left(F^{(1)}, F^{(1)'}\right)$ of the output melt track of the second layer.

The DGP-p model in this study was trained using variational inference combined with stochastic gradient descent. Unlike traditional GP, the multilayer structure of DGP limits the direct computation of the exact posterior distribution. Hence, the variational inference was used to approximate the posterior distribution. The objective function of the model is the evidence lower bound (ELBO).

$$L(\theta) = E_q\left[logp(y \mid F^{(2)})\right] - KL\left[q\left(F^{(1)}\right) \| p(F^{(1)} \mid X_t)\right] - KL\left[q\left(F^{(2)} \mid F^{(1)}\right) \| p(F^{(2)} \mid F^{(1)})\right] \quad \text{(XVII)}$$

Where θ denotes the model learnable parameter.

θ is all learnable parameters.

E_q $[logp(y|F^{(2)})]$ is the expected log-likelihood of y with given $F^{(2)}$.

$q(F^{(1)})$ isthe variational distribution of hidden variables in the first layer.

$q(F^{(2)}/F^{(1)})$ is the conditional variational distribution of second-layer hidden variables given $F^{(1)}$.

$p(F^{(1)}|X_t)$ is the conditional prior distribution of the first-layer latent variable given the input X_t

$p(F^{(2)}|F^{(1)})$ is the conditional prior distribution of the second-layer latent variable given $F^{(1)}$.

KL(·): This function means kullback-leibler divergence.

We using Equation XVII as the loss equation to train the model.

In the optimization process, the Adam optimizer was used for gradient updating. The initial learning rate was set to 0.01, and an exponential decay strategy was used, where the learning rate was decayed to 0.9 times the original rate at every 50 rounds of iterations. To avoid local optima, an early stopping strategy was implemented during training, halting the process when the validation loss fails to improve over 10 consecutive epochs.

After obtaining the predicted melt track geometric features [W_t, D_t, H_t] from the melt pool features, the deviation of the predicted melt track volume Vol_t from the ideal volume V was calculated using Equation XVIII.

$$\Delta V = Vol_t - Vol = \left(\frac{\pi W_t^2}{4} - \frac{1}{2} W_t H_t\right)\sqrt{L^2 + (D_t - D_{t-1})^2} - V \quad \text{(XVIII)}$$

Where L_v is the corresponding track length of the melt pool under different laser scanning speeds.

The deviation characteristics were determined by synthesizing the predicted deviations of track width, height, and position (Equations XIX-XXII).

$$\Delta = [\Delta V, \Delta W, \Delta D, \Delta H] \quad \text{(XIX)}$$

$$\Delta W = W_t - W \quad \text{(XX)}$$

$$\Delta D = D_t - D \quad \text{(XXI)}$$

$$\Delta H = H_t - h \quad \text{(XXII)}$$

Where ΔW, ΔD, and ΔH denote the deviations in melt track width, deviation, and height, respectively.

Based on the deviation features and melt track category labels, a simple and efficient softmax classifier was utilized to classify the melt track categories.

2.6. Model training

During training, the root mean square error (RMSE) (Equation XXIII) was used to evaluate model performance.

$$RMSE = \left(\frac{1}{n}\sum_{i=1}^{n}\left(\bar{f}_i - f_i\right)^2\right)^{0.5} \quad \text{(XXIII)}$$

Where n is the number of samples, $\bar{f}_i$ is the true value, and f_i is the predicted value.

The training effect of the proposed model using RMSE loss in 70 epochs is displayed in Figure 10. During the first 10 epochs, both training and validation losses decreased rapidly in parallel, indicating efficient initial model learning. Between epochs 10 – 40, convergence decreased without oscillation. Beyond epoch 40, while training loss continued to decline, validation loss exhibited slow fluctuations with a gradually widening divergence between them, suggesting mild overfitting.

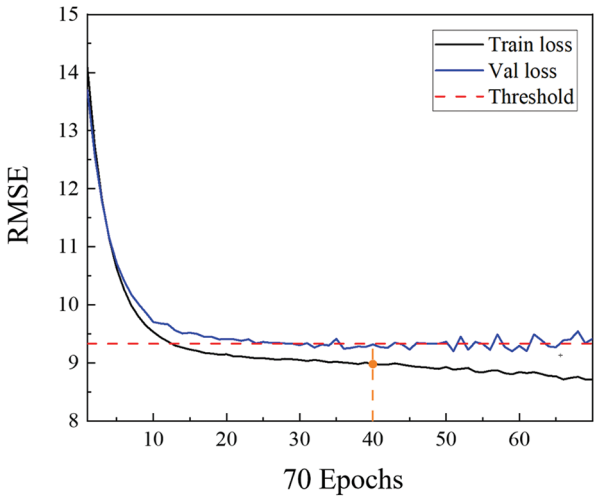

Figure 10. Root mean square error loss of the DGP-p model
Abbreviations: DGP-p: DGP model using physical kernel; Val: Validation datasets; Train: Training datasets

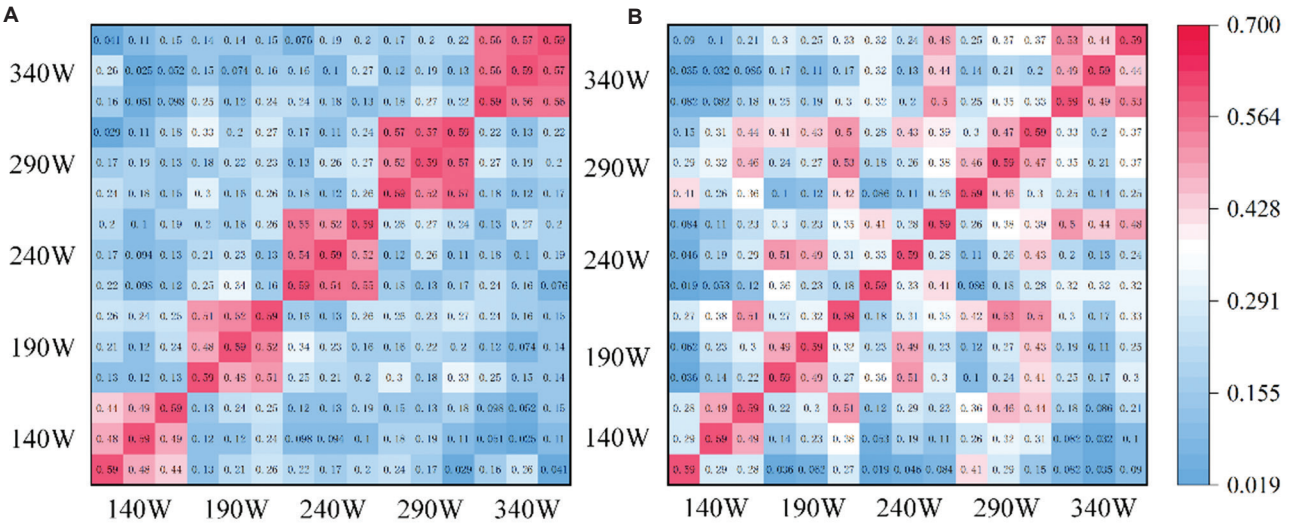

Figure 11. Covariance matrix heat map: (A) DGP-p, and (B) DGP-b
Abbreviations: DGP-p: DGP model using physical kernel; DGP-b: DGP model using basic mahalanobis kernel

Therefore, the model in the 40th epoch was selected as the optimal training model, and the generalization gap of the model at this point was 3.76%, which is within a reasonable range.

To verify the guiding effect of the physical constraint kernel function on the training process, we first selected a test group with a scanning speed of 860 mm/s. We then randomly selected three samples from this test group that had different powers. Next, we compared these three samples using two models: (i) the DGP-b model, which uses an ordinary martensitic kernel, and (ii) the DPG-p model, which employs a physical constraint kernel. Thereafter, we calculated the kernel covariance matrix for each of the comparisons and generated heat maps based on the calculated kernel covariance matrices. The results of this analysis are presented in Figure 11.

Due to data normalization, the constant diagonal values equal 0.59. It can be observed that for the same power group, a high covariance value was obtained; at different power groups, the covariance values were lower; and the intra-group similarity increased with increasing power (Figure 11A). In Figure 11B, the inter-group similarity (0.533) significantly exceeded the intra-group similarity (0.281), with a more dispersed distribution pattern. This indicates that the relationship is governed by data distribution rather than physical laws, failing to reflect the power increment effect.

In addition, the stability of working conditions was improved, and some of the cross-group covariance values were high, with noise interference. This result indicates that the physical kernel effectively suppresses unphysical fluctuations – resulting in high similarity within the same power group and low similarity across groups – and noise interference.

Table 1. Ablation experimental prediction results

Prediction set	Geometric features	Root mean square error	
		DGP-p	DGP-b
240 W-660 mm/s	Width	0.060	0.068
	Deviation	0.020	0.023
	Height	0.043	0.047
290 W-760 mm/s	Width	0.065	0.090
	Deviation	0.017	0.023
	Height	0.036	0.039
340 W-960 mm/s	Width	0.083	0.121
	Deviation	0.024	0.031
	Height	0.038	0.040

Note: The geometric features were evaluated based on the root mean square error.
Abbreviation: DGP: Deep Gaussian processes

3. Results and discussion

3.1. Interpretability based on physical constraints

To verify the effectiveness of the proposed physically constrained martensitic kernel, the results of the DGP-b and DGP-p models on the prediction set were compared (Table 1).

As observed from Table 1, the DGP-p model – using a physically constrained martensitic kernel—has a lower average relative error than the DGP-b model – using the

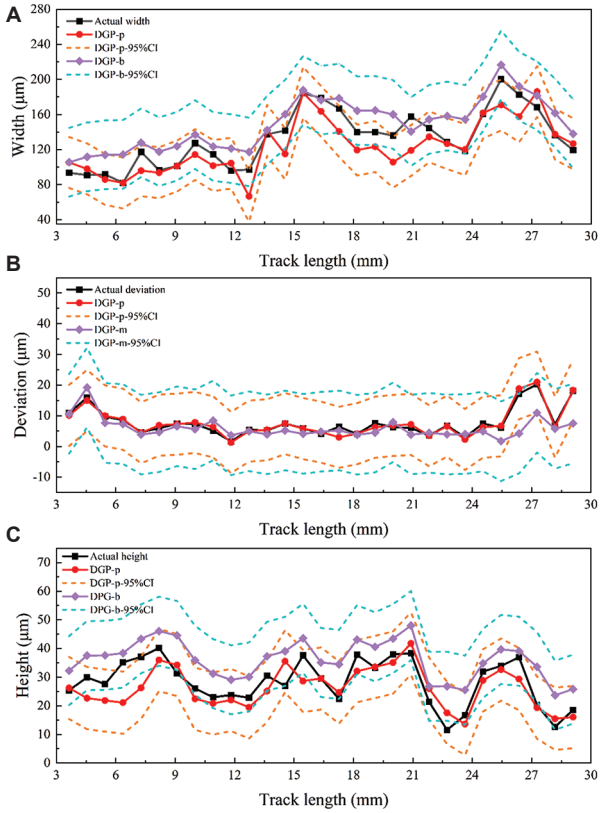

Figure 12. Ablation experiment: (A) width, (B) deviation, and (C) height Abbreviations: DGP-p: DGP model using physical kernel; DGP-b: DGP model using basic mahalanobis kernel; CI: Confidence interval

standard martensitic kernel. The average improvement in width, deviation, and height are 23.65%, 20.57%, and 7.07%, respectively. The prediction curves of the ablation test are presented in Figure 12. Further analysis of the width of the confidence intervals revealed a smaller confidence interval for the DGP-p model compared to the DGP-b model; the mean widths of the confidence intervals (width, deviation, and height) for the DGP-p model decreased from 39.170 μm, 12.970 μm, and 12.051 μm to 37.579 μm, 9.957 μm, and 10.858 μm, respectively. This result indicates that the physical constraints reduced the prediction uncertainty.

The prediction mean of the DGP-b model is generally higher than that of the DGP-p model, as the ordinary martensitic kernel relies on training data statistics, which may maintain a statistically positive correlation between power and track size. However, due to complex non-linear relationships in actual processing, such as melt pool mode shifts under high power conditions,[16] the real track size grows slowly. The martensitic kernel fails to constrain this non-linear decoupling, resulting in overprediction.

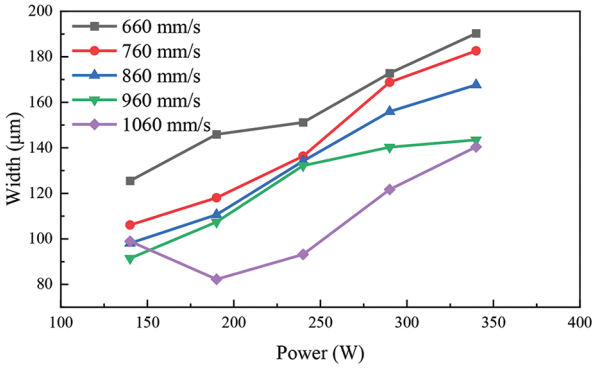

Figure 13. Width of the melt track

The physical kernel forces the model to follow the non-linear equilibrium between power, velocity, and track size through Rosenthal's equation, effectively limiting excessive growth of the predicted width and height. The specific widths of each group of tracks under this test are displayed in Figure 13. At a fixed scanning speed, the track width growth rate decreased with increasing laser power.

3.2. Comparison of melt track size prediction

We evaluated the prediction performance using four models, namely, the elasticity regression model (ENR), GP regression model, support vector machines (SVR), and Kolmogorov-Arnold Networks (KAN). ENR is a classical linear regression model and was used in this study to compare the applicability of the linear model with the non-linear model in predicting the melt track geometric features. GP was used to verify whether this experiment required a DGP model with multiple layers and multiple parallel GPs per layer to manage the complex non-linear relationship between melt pool geometric features and melt track geometric features. SVR is an algorithm that solves non-linear problems using kernel functions. KAN is a model proposed in recent years that implements non-linear modeling using the Kolmogorov-Arnold theorem. The selection of DGP is justified by comparing these algorithms, each with different characteristics.

Both ENR and SVR were implemented based on the Sklearn framework, while GP, KAN, and DGP were implemented based on the Pytorch framework. The basic parameters of the model were set as follows:

(i) ENR: The L1 regularization ratio was set at 45%; the L2 regularization ratio was set at 55%; the learning rate adopted the auto-tuning strategy; and the number of iterations was set to 50.

(ii) GP: The Matérn kernel was used; the smoothing parameter was set to 2.5; the remaining hyperparameters were set to 1; and the mean function was constant.

(iii) SVR: The radial basis kernel function was used and the regular term coefficient was set to 1.
(iv) KAN: Three hidden layers were used; the number of neurons was 36, 24, and 12, respectively, connected by fully connected form; the number of iterations was 100; the optimizer used Adam; and the learning rate was set to 0.001.
(v) DGP-p: The first layer used a Gaussian cosine composite kernel, with a smoothing parameter set to 2.5 and the period set to 1; the second layer used a physically constrained Matérn kernel.

Table 2 presents the average RMSE of the model predictions for the three sets of experiments computed using MinMax-normalized data.

Table 2. Experimental prediction results

Experimental set	Geometric features	Root mean square error				
		DGP	GP	KAN	SVR	ENR
240 W-660 mm/s	Width	0.060	0.288	0.268	0.236	0.234
	Deviation	0.020	0.097	0.057	0.124	0.150
	Height	0.043	0.053	0.047	0.048	0.048
290 W-760 mm/s	Width	0.065	0.170	0.157	0.136	0.141
	Deviation	0.017	0.121	0.032	0.044	0.045
	Height	0.036	0.062	0.050	0.054	0.044
340 W-960 mm/s	Width	0.083	0.201	0.174	0.136	0.151
	Deviation	0.024	0.041	0.055	0.049	0.045
	Height	0.038	0.067	0.069	0.052	0.061

Note: The geometric features were evaluated based on the root mean square error.
Abbreviations: DGP: Deep Gaussian processes; GP: Gaussian processes; KAN: Kolmogorov-Arnold Networks; SVR: Support vector machines; ENR: Elasticity regression model.

From the model RMSE results, the DGP – optimized based on the physical model – significantly outperformed the GP, KAN, SVR, and ENR models in the prediction of melt track geometric features. To further elucidate the rationale for selecting the DGP model, the 340 W-960 m/s experimental set with the largest RMSE index was further analyzed. Figures 14-16 demonstrate that when back-normalizing true values to predicted values, the RMSE differences between models in the experimental set are minimal. However, the melt track exhibits reduced widths in initial segments and increased fluctuation amplitudes during mid-to-late stages.

In the width prediction of the melt track (Figure 14), there were some gaps between the SVR model and the actual melt track width at the beginning, with notable hysteresis at width value fluctuations. There was a bigger gap between the KAN model and the actual melt track width at the beginning, and there were fluctuations in the width value. The prediction result of the ENR model was relatively smooth, which does not conform to the fluctuation of the actual width. The prediction result of the GP model was relatively good in the initial stage, with a decent width in the tail section. While the GP model achieved precise front-section width predictions, its tail-section predictions diverged substantially from experimental data. This discrepancy correlates with observed hysteresis in tracking time-dependent width variations, indicating limited dynamic response capability.

In the deviation prediction of the melt track (Figure 15), the SVR model displayed better prediction results in the middle and end sections and appeared to be more sensitive to the sudden fluctuation of the melt track deviation. The KAN and ENR models demonstrated relatively smooth

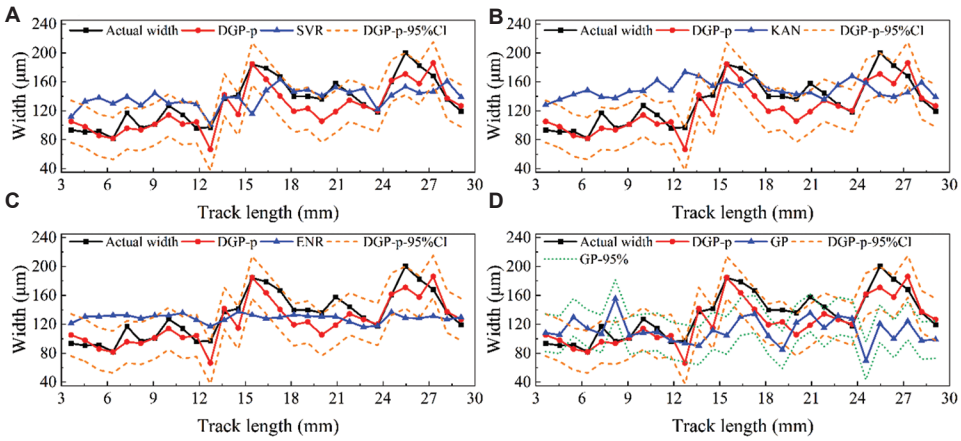

Figure 14. Comparison of validation results between the proposed DGP model and various other models in width prediction: (A) SVR, (B) KAN, (C) ENR, and (D) GP
Abbreviations: DGP-p: DGP model using physical kernel; ENR: Elasticity regression model; GP: Gaussian process regression model; SVR: Support vector machines

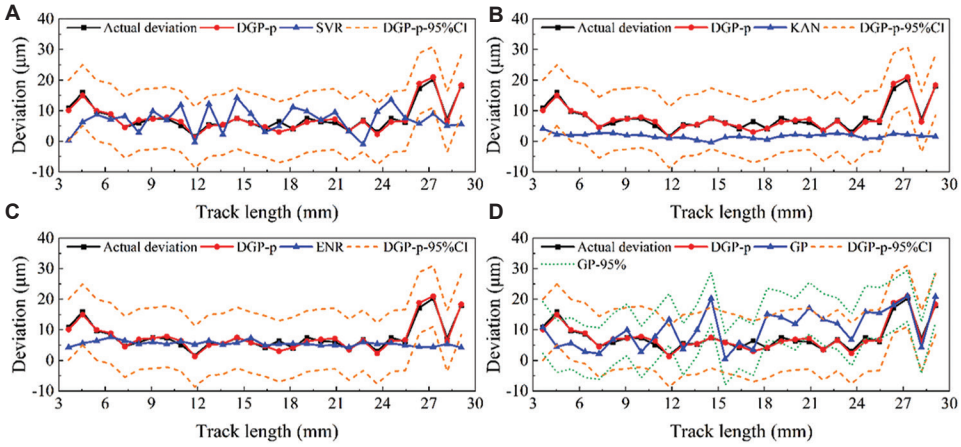

Figure 15. Comparison of validation results between the proposed DGP model and various other models in deviation prediction: (A) SVR, (B) KAN, (C) ENR, and (D) GP
Abbreviations: DGP-p: DGP model using physical kernel; ENR: Elasticity regression model; GP: Gaussian process regression model; SVR: Support vector machines

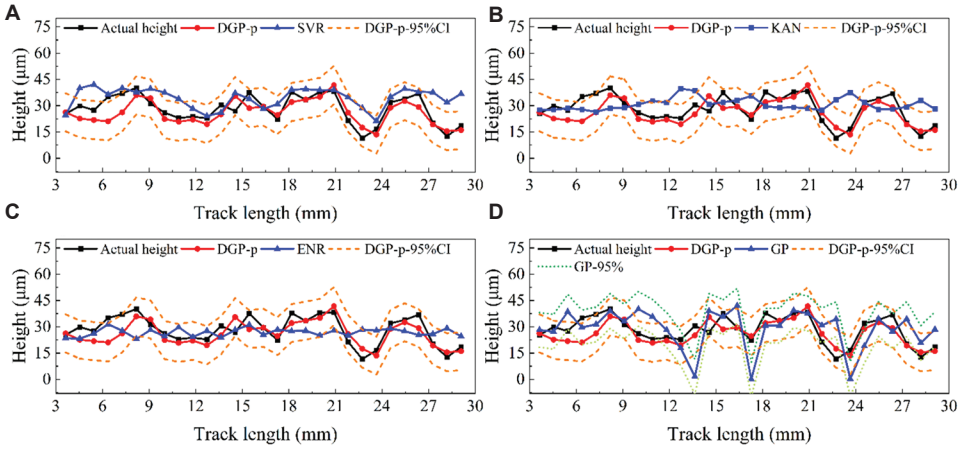

Figure 16. Comparison of validation results between the proposed DGP model and various other models in height prediction: (A) SVR, (B) KAN, (C) ENR, and (D) GP
Abbreviations: DGP-p: DGP model using physical kernel; ENR: Elasticity regression model; GP: Gaussian process regression model; SVR: Support vector machines

deviation fluctuations and were not sensitive to the sudden fluctuation of the melt track deviation. The GP model presented a stronger fluctuation and appeared to be more sensitive to the fluctuation of the melt track deviation.

In the height prediction of the melt track (Figure 16), the SVR model predicted changes that aligned with the changes in the real value. The KAN and ENR models displayed relatively smooth height fluctuations and were not sensitive to the sudden fluctuation of the melt track height. The GP model demonstrated strong volatility and was more sensitive to the fluctuation of the melt track height.

Overall, in predicting the geometric characteristics of the melt track, the linear ENR model demonstrates fundamental limitations by capturing only global linear relationships while failing to model non-linear melt pool dynamics. Comparatively, non-linear models reveal critical constraints. For instance, the KAN model – bound by the univariate superposition principle of Kolmogorov-Arnold's theorem – inadequately represents higher-order non-linear coupling that is inherent in melt track feature interdependencies. This theoretical limitation, combined with poor local mutation modeling capacity, results in KAN's inferior performance among the non-linear models.

The GP model directly models data distributions through covariance, but risks performance degradation from kernel overfitting noise and sensitivity to data

sparsity. In contrast, the SVR model achieves superior performance by balancing global trend capture with moderate local mutation sensitivity. The DGP-based melt track geometric feature prediction model is guided by multilayer non-linear hidden variable transfer and physical principles, ensuring the capability to accommodate sudden local offsets while predicting global trends. This approach mitigates purely data-driven overfitting risks, enforces physical law compliance in predictions, and enhances model interpretability. Due to its multilayer architecture, uncertainty propagates layer-wise through kernel functions from initially hidden variables, resulting in marginally expanded confidence intervals compared to traditional GP models.

However, the impact of the transmission of uncertain hidden variables is significantly reduced through the introduction of physical constraints. The predicted average width of the melt track was 123.55 μm and the average height was 28.29 μm, comparable to the actual geometry of the melt track by 9.89% and 16.03%, respectively, with a relative error of 10.21% in the average deviation. The relative errors in the width, height, and deviation predictions for the other groups were 8.06%, 14.45%, and 9.59% (for 240 W-660 mm/s) and 8.13%, 11.60%, and 9.39% (for 290 W-760 mm/s), with average relative errors of 8.69%, 14.02%, and 9.73%, respectively.

The DGP model demonstrates the highest accuracy in melt track width prediction. However, deviation predictions deteriorate significantly, while height predictions display the poorest performance. Notably, under higher energy density, the 24th group (refers to 340 W-960 mm/s) exhibited larger average relative errors than the other two groups. This degradation may be attributable to three factors: (i) the melt pool behavioral pattern changes under high power, invalidating Equation X to this process parameter; (ii) the assumption of Equation IX on the height is relatively simple and does not sufficiently take into account the actual physical process; and (iii) the height of the melt track is sensitive to changes in the melt pool aspect ratio, and the optimal time lag value of the melt pool aspect ratio is 2, resulting in deterioration in the prediction effect.

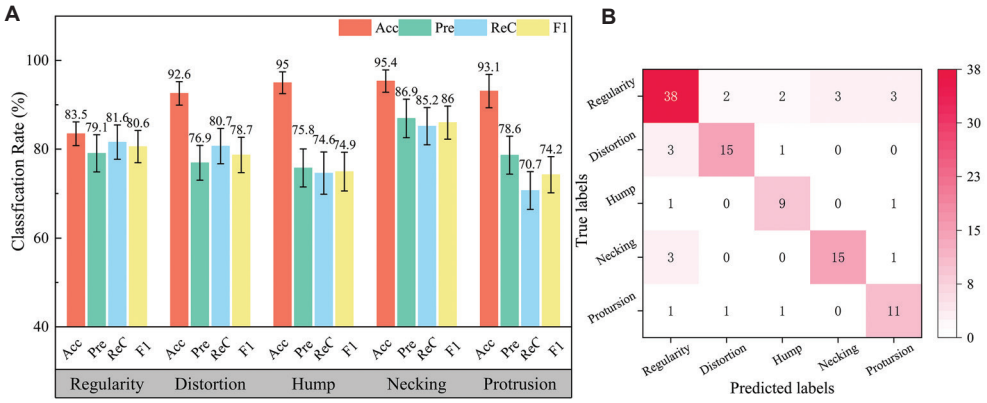

Figure 17. Classification results without oversampling: (A) evaluation metrics; and (B) confusion matrix

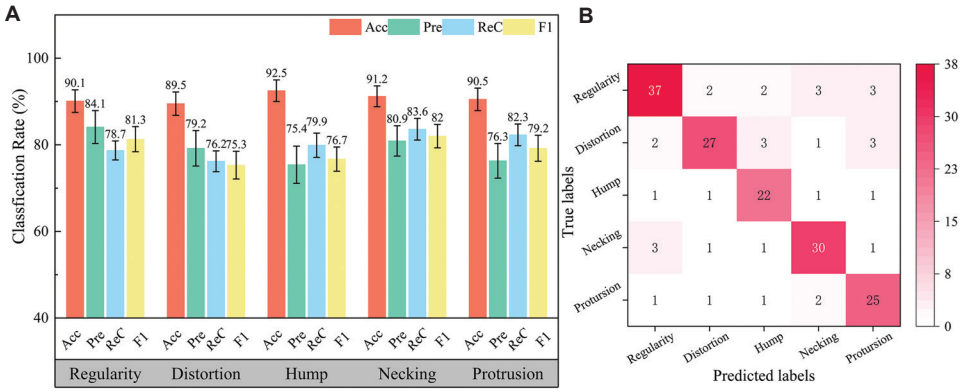

Figure 18. Classification results with oversampling: (A) evaluation metrics, and (B) confusion matrix

3.3. Morphological prediction

Following physical constraint-guided DGP model predictions of melt track dimensions, the deviation feature (Equation XIX) was used to predict the melt track morphology (Figure 17). This approach demonstrates robust predictive performance based on quantification by accuracy (91.89%), precision, recall, and F1-score metrics.

Analysis of evaluation metrics (Figure 17A) and the confusion matrix (Figure 17B) revealed sample imbalance across defect categories. To address this, two-stage SMOTE oversampling was applied to the five defect classes, consequently generating improved predictions (Figure 18).

A comparison between Figures 17A and 18A reveals significant recall improvements of 5.3% and 11.6% in the hump and protrusion categories, respectively. In addition, the standard deviation decreased across all categories, while the model's predictive consistency improved. Although the model exhibited reduced precision and fluctuations in accuracy, its substantial enhancement in defect detection recall demonstrates satisfactory overall performance.[38]

Similarly, a comparison between Figures 17B and 18B reveals a notably high leakage rate (exceeding 16%) in the regularity category, which is prone to confusion with other defect types, and may also affect other defect categories. The issue could be due to the presence of composite defect morphologies within the melt tracks, as exemplified by the three typical cases displayed in Figure 19. Specifically, the composite necking-protrusion morphology can produce an average melt track width similar to that of the regularity category in the final sampling results. Since the classifier relies primarily on global features and overlooks local feature mutations, classification boundaries become blurred, leading to misses (leakage) and false positives. Consequently, enhancing the classifier's ability to accurately recognize multiple co-occurring defects within a single melt track remains a significant challenge.

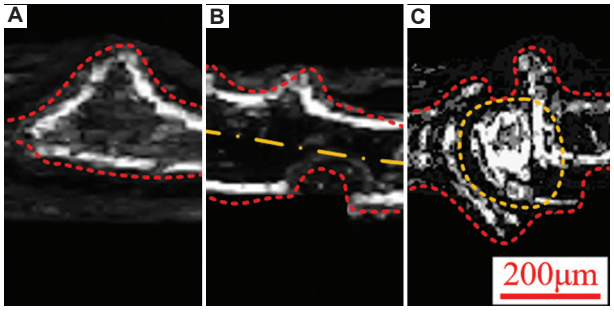

Figure 19. Composite morphology. (A) necking-protrusion. (B) distortion-necking-protrusion. (C) hump-protrusion. Scale bar: 200 μm

These findings further indicate that samples from different morphology categories occupy overlapping regions in the feature space, leading to confusion and ambiguous classification boundaries.

To understand the importance of different deviations for the class prediction of melt tracks, a feature importance analysis method based on permutation importance was used to verify whether the physical model of the theoretical deviations of melt tracks can effectively distinguish the classes of different melt track morphologies. Figure 20A demonstrates the importance of different deviations in the prediction of categories, and Figure 20B demonstrates the volumetric deviations on the upper surface of the melt track for different categories. These findings indicate distributional overlap among different morphology categories in the feature space, resulting in ambiguous classification boundaries and misclassifications. However, volumetric deviation demonstrates the discriminative capability for melt track morphology to some extent, with its high feature importance confirming its role as a critical classifier for morphology differentiation. The corresponding melt track deviation and height deviation values become particularly important for distortion and

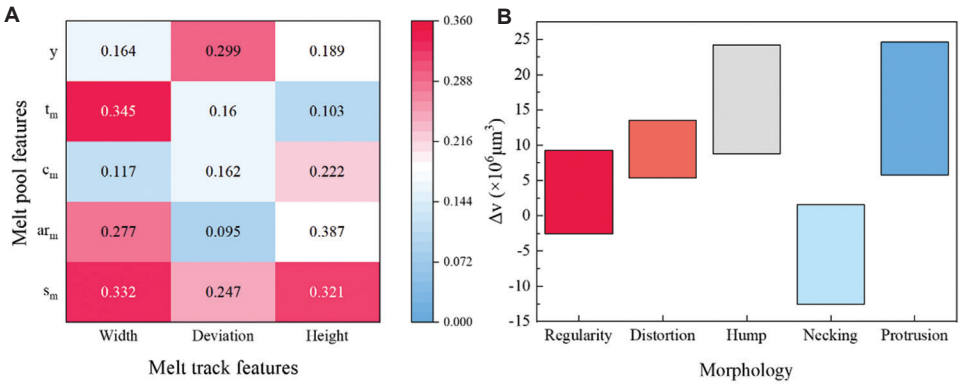

Figure 20. Analysis of classification results: (A) importance of features, and (B) melt track volume deviation

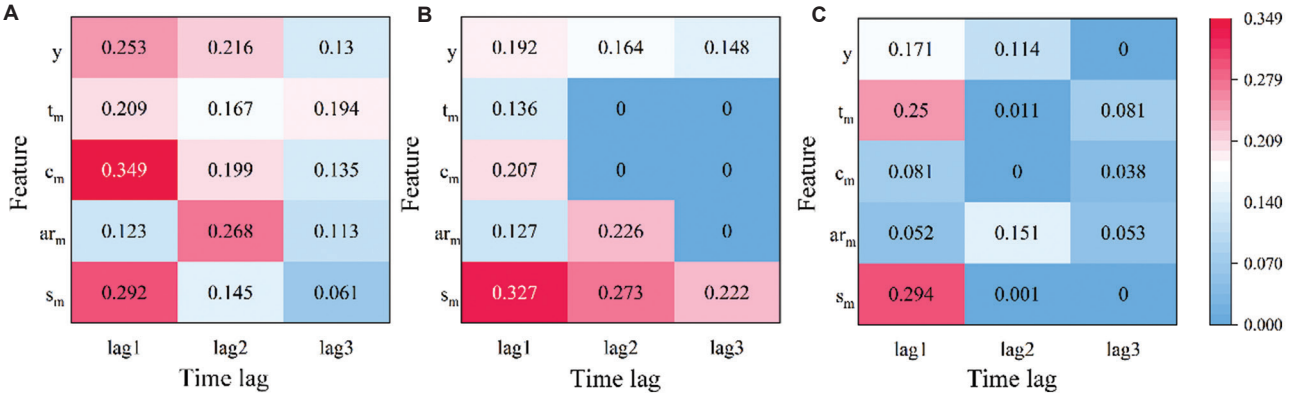

Figure 21. Delay mutual information matrix: (A) melt track width, (B) melt track deviation, and (C) melt track height

hump, which are two defective morphologies mainly caused by melt track deviation and height variation.

3.4. Analysis of the correlation between the melt pool and melt track

To test the hypotheses established in Section 2.3 and further clarify the type of melt pool fluctuations most likely to cause specific defects, the feature-defect causality needs to be quantified. However, Granger's causality analysis[39] is a parametric-based causality analysis method and does not apply to the non-parametric DGP model in this study. Hence, time-lagged mutual information was used instead of the Granger method to evaluate the feature-to-feature non-linear correlations, avoiding the limitations of the linearity assumption and quantifying the dynamic sensitivity.

$$I\left(X_t;Y_{t+\tau}\right)=\sum_{X,Y}p(X_t,Y_{t+\tau})log\frac{p\left(X_t,Y_{t+\tau}\right)}{p\left(X_t\right)p\left(Y_{t+\tau}\right)} \quad \text{(XXIV)}$$

$$S(X_t \to Y_{t+\tau}) = I(X_t; Y_{t+\tau}) - I(X_{t-1}; Y_{t+\tau}) \quad \text{(XXV)}$$

$I(X_t; Y_{t+\tau})$ is the time lag mutual information value between X_t and $Y_{t+\tau}$.

X_t is the eigenvector of the melt pool at time t.

$X_t = \left[s_m^t, ar_m^t, c_m^t, t_m^t, y^t\right]$, The upper right label of the eigenvalue represents the corresponding time t

Y_t is the eigenvector of the melt track at time t, $Y_t = [W_t, D_t, H_t]$

τ is the time lag, $p(X_t, Y_{t+\tau})$ is the joint probability distribution. $p(X_t)$ and $p(Y_{t+\tau})$ are the marginal probability distributions.

$S(X_t \to Y_{t+\tau})$ is the amount of information transmitted from X_t to $Y_{t+\tau}$.

Based on Equation XXIV and Equation XXV, the specific values in each matrix of Figure 21 can be calculated.

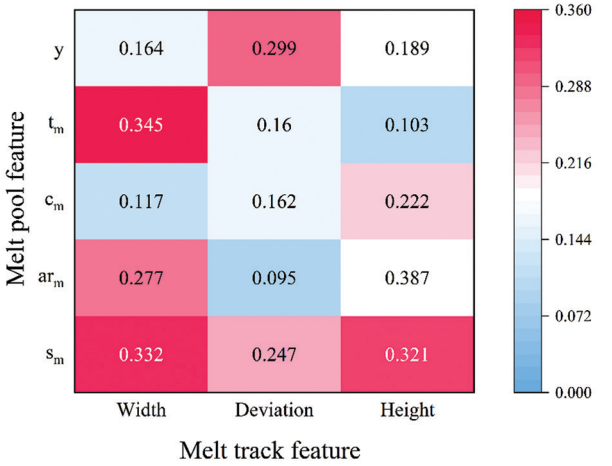

Figure 22. Feature sensitivity matrix

For the melt track geometric features, the time-lag information of the melt pool (melt track width, deviation, and height) is presented in Figure 17, where a larger mutual information value indicates a stronger correlation between the features. Figure 21A demonstrates that the mutual information values of melt track width exhibited a smoother time-lag decay characteristic, and there is a continuous influence of melt pool features on melt track width. Figure 21B highlights that the mutual information values of melt track deviation featured a steep decay trend – especially the mutual information values for c_m and t_m dropping to 0 at lag2 and lag3 – thereby indicating that the effect is limited to the short term. Figure 21C demonstrates that the mutual information value of melt track height is lower than the other two features as a whole, and the s_m and t_m features of the melt pool displayed a strong correlation at lag1, while the values of most features increased at lag3. Most of the features have the highest mutual information value at lag1, while only the ar_m feature of the melt pool has the highest mutual information value at lag2. These results validate the short-term changes of the melt pool feature through the neighboring time series.

Figure 22 displays the sensitivity of the melt track characteristics to changes in the characteristics of the melt pool. Changes in the convexity of the melt pool and the roundness of the melt track are strongly correlated with variations in melt track width, while melt track offset primarily responds to shifts in the melt pool's centroid position and area. In addition, melt track height fluctuations are dependent on alterations to the melt pool's aspect ratio and area. This observation validates the defect-causation hypothesis proposed in Section 2.3. Analysis of the time-lag mutual information matrix further reveals near-synchronized responses between melt track width and deviation changes, whereas height adjustments exhibit a measurable temporal lag.

4. Conclusion

The proposed DGP-p model establishes an interpretable feature-mapping mechanism. Experimental results demonstrate that the physical kernel function enhances intra-group sample variance within the same power category (from 0.456 to 0.547, an improvement of 19.9%) while reducing inter-group covariance across different power categories (from 0.256 to 0.176, a reduction of 31.3%), thereby validating its effectiveness in filtering non-physical feature correlations.

The model demonstrated superior performance under single-sensor conditions, with average relative errors of 9.89% (width), 10.21% (deviation), and 16.03% (height), outperforming traditional machine learning methods. With a 9.8 ms inference time (GPU: 4070super) – slightly slower than the GP model's 7.5 ms – it achieved 65.57% higher prediction accuracy. The melt track defect classifier – combining volumetric deviation (weight = 0.39) and geometric features – attained 90.76% classification accuracy.

This study employed feature-sensitive analysis and time-lag mutual information quantification. Notably, there is a continuous effect of the dynamic behavior of the melt pool on the geometrical characteristics of the melt track: the melt track width is affected by the convexity characteristics of the melt pool and the area. The deviation of the melt track is affected by the position of the center of mass and the area of the melt pool, while the height of the melt track is affected by the length-to-width ratio of the melt pool and the area.

Overall, this study highlights that there is a continuous effect on the changes induced by these features, with a significant lag effect on the changes induced by the melt pool aspect. Based on these findings, an effective early warning mechanism can be established at the early stages of defect formation by monitoring changes in the geometric features of the melt pool in real time. This study provides a reference for AM process monitoring and defect prevention and control. Future research will further investigate how single-track defects propagate through multilayer and multi-track interactions.

Acknowledgments

The authors would like to acknowledge financial support from the National Natural Science Foundation of China under Grant Number 52175481 and the China Post-doctoral Science Foundation under Grant Number 2023M743539.

Funding

This work was supported in part by the National Natural Science Foundation of China (grant no. 52175481) and in part by the China Post-doctoral Science Foundation (grant no. 2023M743539).

Conflict of interest

Xin Lin serves as the Editorial Board Member of the journal but was not in any way involved in the editorial and peer-review process conducted for this paper, directly or indirectly. Other authors declare they have no competing interests.

Author contributions

Conceptualization: Xin Lin and Kunpeng Zhu
Formal analysis: Xin Lin
Investigation: Xin Lin, Kunpeng Zhu, and Haodong Chen
Methodology: Shilin Liu, Xin Lin, Kunpeng Zhu, and Jinrong Mao
Writing – original draft: Shilin Liu, Haodong Chen, and Xin Lin
Writing – review and editing: Xin Lin

Ethics approval and consent to participate

Not applicable.

Consent for publication

Not applicable.

Availability of data

The raw/processed data required to reproduce these findings cannot be shared at the time of publication, as the data also forms part of an ongoing study.

References

1. Khairallah SA, Martin AA, Lee JR, *et al.* Controlling interdependent meso-nanosecond dynamics and defect generation in metal 3D printing. *Science.*

2020;368(6491):660-665.

doi: 10.1126/science.aay7830

2. Fang Q, Tan Z, Li H, *et al*. *In-situ* capture of melt pool signature in selective laser melting using U-Net-based convolutional neural network. *J Manuf Process*. 2021;68:347-355.

doi: 10.1016/j.jmapro.2021.05.052

3. Yang L, Lo L, Ding S, Özel T. Monitoring and detection of meltpool and spatter regions in laser powder bed fusion of super alloy Inconel 625. *Prog Addit Manuf*. 2020;5(4):367-378.

doi: 10.1007/s40964-020-00140-8

4. Liu J, Wei B, Chang H, Li J, Yang G. Review of visual measurement methods for metal vaporization processes in laser powder bed fusion. *Micromachines (Basel)*. 2023;14(7):1351.

doi: 10.3390/mi14071351

5. Forien JB, Calta NP, DePond PJ, Guss GM, Roehling TT, Matthews MJ. Detecting keyhole pore defects and monitoring process signatures during laser powder bed fusion: A correlation between *in situ* pyrometry and *ex situ* X-ray radiography. *Addit Manuf*. 2020;35:101336.

doi: 10.1016/j.addma.2020.101336

6. Khanzadeh M, Chowdhury S, Tschopp MA, Doude HR, Marufuzzaman M, Bian L. *In-situ* monitoring of melt pool images for porosity prediction in directed energy deposition processes. *IISE Trans*. 2018;51(5):437-455.

doi: 10.1080/24725854.2017.1417656

7. Khanzadeh M, Dantin M, Tian W, Priddy MW, Doude H, Bian L. Fast prediction of thermal data stream for direct laser deposition processes using network-based tensor regression. *J Manuf Sci Eng*. 2021;144(4):041004.

doi: 10.1115/1.4052207

8. Scime L, Beuth J. Anomaly detection and classification in a laser powder bed additive manufacturing process using a trained computer vision algorithm. *Addit Manuf*. 2018;19:114-126.

doi: 10.1016/j.addma.2017.11.009

9. Okaro IA, Jayasinghe S, Sutcliffe C, Black K, Paoletti P, Green PL. Automatic fault detection for laser powder-bed fusion using semi-supervised machine learning. *Addit Manuf*. 2019;27:42-53.

doi: 10.1016/j.addma.2019.01.006

10. Yuan B, Giera B, Guss G, Matthews M, McMains S. Semi-supervised convolutional neural networks for *in-situ* video monitoring of selective laser melting. In: *2019 IEEE Winter Conference on Applications of Computer Vision (WACV)*. United States: IEEE; 2019. p. 744-753.

doi: 10.1109/WACV.2019.00084

11. Yuan B, Guss GM, Wilson AC, *et al*. Machine-learning-based monitoring of laser powder bed fusion. *Adv Mater Technol*. 2018;3(12):1800136.

doi: 10.1002/admt.201800136

12. Mojahed Yazdi R, Imani F, Yang H. A hybrid deep learning model of process-build interactions in additive manufacturing. *J Manuf Syst*. 2020;57:460-468.

doi: 10.1016/j.jmsy.2020.11.001

13. Lopez F, Witherell P, Lane B. Identifying uncertainty in laser powder bed fusion additive manufacturing models. *J Mech Des*. 2016;138(11):114502.

doi: 10.1115/1.4034103

14. Mahmoudi M, Ezzat A, Elwany A. Layerwise anomaly detection in laser powder-bed fusion metal additive manufacturing. *J Manuf Sci Eng*. 2019;141(3):031002.

doi: 10.1115/1.4042108

15. Gaikwad A, Giera B, Guss GM, Forien JB, Matthews MJ, Rao P. Heterogeneous sensing and scientific machine learning for quality assurance in laser powder bed fusion - a single-track study. *Addit Manuf*. 2020;36:101659.

doi: 10.1016/j.addma.2020.101659

16. Guo K, Qiao L, Huang Z, Anwer N, Cao Y. A computational model of melt pool morphology for selective laser melting process. *Int J Adv Manuf Technol*. 2022;121(3-4):1651-1673.

doi: 10.1007/s00170-022-09366-y

17. Zhang H, Vallabh CK, Zhao X. Registration and fusion of large-scale melt pool temperature and morphology monitoring data demonstrated for surface topography prediction in LPBF. *Addit Manuf*. 2022;58:103075.

doi: 10.1016/j.addma.2022.103075

18. Biggio L, Wieland A, Chao MA, Kastanis I, Fink O. Uncertainty-aware prognosis via deep gaussian process. *IEEE Access*. 2021;9:123517-123527.

doi: 10.1109/ACCESS.2021.3110049

19. Fan Z, Lu M, Huang H. Selective laser melting of alumina: A single track study. *Ceram Int*. 2018;44(8):9484-9493.

doi: 10.1016/j.ceramint.2018.02.166

20. Yadroitsev I, Krakhmalev P, Yadroitsava I, Johansson S, Smurov I. Energy input effect on morphology and microstructure of selective laser melting single track from metallic powder. *J Mater Process Technol*. 2013;213(4):606-613.

doi: 10.1016/j.jmatprotec.2012.11.014

21. Yang J, Liu G, Zhu W, *et al*. High-precision and ultraspeed monitoring of melt-pool morphology in laser-directed energy deposition using deep learning. *Addit Manuf Front*. 2025;4(2):200199.

doi: 10.1016/j.amf.2025.200199

22. Xiang Y, Zhang S, Wei Z, *et al*. Forming and defect analysis for single track scanning in selective laser melting of Ti6Al4V. *Appl Phys A*. 2018;124(10):685.

doi: 10.1007/s00339-018-2056-9

23. Hu Z, Nagarajan B, Song X, Huang R, Zhai W, Wei J. Formation of SS316L single tracks in micro selective laser melting: Surface, geometry, and defects. *Adv Mater Sci Eng*. 2019;2019:9451406.

doi: 10.1155/2019/9451406

24. Zhou H, Su H, Guo Y, *et al*. Formation and evolution of surface morphology in overhang structure of IN718 superalloy fabricated by laser powder bed fusion. *Acta Metall Sin*. 2023;36(9):1433-1453.

doi: 10.1007/s40195-023-01546-3

25. Li C, Guo YB, Zhao JB. Interfacial phenomena and characteristics between the deposited material and substrate in selective laser melting Inconel 625. *J Mater Process Technol*. 2017;243:269-281.

doi: 10.1016/j.jmatprotec.2016.12.033

26. Khairallah SA, Anderson AT, Rubenchik A, King WE. Laser powder-bed fusion additive manufacturing: Physics of complex melt flow and formation mechanisms of pores, spatter, and denudation zones. *Acta Mater*. 2016;108:36-45.

doi: 10.1016/j.actamat.2016.02.014

27. Chen H, Lin X, Sun Y, Wang S, Zhu K, Dan B. Revealing formation mechanism of end of process depression in laser powder bed fusion by multi-physics meso-scale simulation. *Virtual Phys Prototyp.* 2024;19(1):e2326599.

doi: 10.1080/17452759.2024.2326599

28. Yuan P, Gu D. Molten pool behaviour and its physical mechanism during selective laser melting of TiC/AlSi10Mg nanocomposites: Simulation and experiments. *J Phys D Appl Phys.* 2015;48(3):035303.

doi: 10.1088/0022-3727/48/3/035303

29. Yuan W, Chen H, Cheng T, Wei Q. Effects of laser scanning speeds on different states of the molten pool during selective laser melting: Simulation and experiment. *Mater Des*. 2020;189:108542.

doi: 10.1016/j.matdes.2020.108542

30. Caprio L, Demir A, Previtali B. Observing molten pool surface oscillations during keyhole processing in laser powder bed fusion as a novel method to estimate the penetration depth. *Addit Manuf*. 2020;36:101470.

doi: 10.1016/j.addma.2020.101470

31. Tang M, Pistorius PC, Beuth JL. Prediction of lack-of-fusion porosity for powder bed fusion. *Addit Manuf*. 2017;14:39-48.

doi: 10.1016/j.addma.2016.12.001

32. Ning J, Mirkoohi E, Dong Y, Sievers DE, Garmestani H, Liang SY. Analytical modeling of 3D temperature distribution in selective laser melting of Ti-6Al-4V considering part boundary conditions. *J Manuf Process*. 2019;44:319-326.

doi: 10.1016/j.jmapro.2019.06.013

33. Promoppatum P, Yao SC, Pistorius PC, Rollett AD. A comprehensive comparison of the analytical and numerical prediction of the thermal history and solidification microstructure of inconel 718 products made by laser powder-bed fusion. *Engineering*. 2017;3(5):685-694.

doi: 10.1016/J.ENG.2017.05.023

34. Wang W, Liang SY. A 3D analytical modeling method for keyhole porosity prediction in laser powder bed fusion. *Int J Adv Manuf Technol*. 2022;120(5-6):3017-3025.

doi: 10.1007/s00170-022-08898-7

35. Yang J, Han J, Yu H, *et al*. Role of molten pool mode on formability, microstructure and mechanical properties of selective laser melted Ti-6Al-4V alloy. *Mater Des*. 2016;110:558-570.

doi: 10.1016/j.matdes.2016.08.036

36. Kamath C, El-dasher B, Gallegos GF, King WE, Sisto A. Density of additively-manufactured, 316L SS parts using laser powder-bed fusion at powers up to 400 W. *Int J Adv Manuf Technol*. 2014;74(1-4):65-78.

doi: 10.1007/s00170-014-5954-9

37. Salimbeni H, Deisenroth M. Doubly stochastic variational inference for deep Gaussian processes. In: *Advances in Neural Information Processing Systems*. United States: Morgan Kaufmann Publishers Inc.; 2017. p. 30.

doi: 10.48550/arXiv.1705.08933

38. Roth K, Pemula L, Zepeda J, Scholkopf B, Brox T, Gehler P. Towards total recall in industrial anomaly detection. In: *IEEE/CVF Conference on Computer Vision and Pattern Recognition (CVPR)*. United States: IEEE; 2022. p. 14298-14308.

doi: 10.1109/cvpr52688.2022.01392

39. Shojaie A, Fox EB. Granger causality: A review and recent advances. *Annu Rev Stat Appl.* 2022;9(1):289-319.

doi: 10.1146/annurev-statistics-040120-010930